



# Room temperature ammonia gas sensor using Nd-doped SnO<sub>2</sub> thin films and its characterization

S. Maheswari<sup>1,2</sup> · M. Karunakaran<sup>2</sup> · L. Bruno Chandrasekar<sup>3</sup> · K. Kasirajan<sup>2</sup> · N. Rajkumar<sup>4</sup>

Received: 10 April 2020 / Accepted: 13 June 2020 / Published online: 22 June 2020  
© Springer Science+Business Media, LLC, part of Springer Nature 2020

## Abstract

Nd-doped SnO<sub>2</sub> thin films are prepared by the nebulizer spray pyrolysis method. The compositional and morphological studies are discussed. The X-ray diffraction reveals that the films are polycrystalline in nature. The grain size increases as the doping concentration of Nd increases. The x-axis orientation of the films is enhanced by Nd doping. The intensity of the miller indices (200) is enhanced due to doping. In the Raman spectrum, the doping concentration-dependent intensity is observed. The quenching is observed in the photoluminescence spectrum. The transmittance and the band gap of films have been decreased due to doping. The 5 wt% Nd-doped film shows the maximum response to ammonia.

## 1 Introduction

The study and analysis of low-dimensional semiconductors are one of the important studies in science and technology throughout the world [1–3]. The metal oxide semiconductors show high electrical conductance with high transparency in the visible region which have the applications in solar cell, light-emitting diodes, and other optoelectronic devices [4]. In the metal oxide group semiconductors, tin oxide is one of the notable semiconductors and has a wide band gap with high transparency in the visible region [5]. The research about tin oxide semiconductor is encouraged due to the potential applications such as gas sensors, light-emitting diodes, and solar cell windows [6–9]. Recently, antimony, phosphorus, zinc, strontium, fluorine, nickel, and zirconium-doped SnO<sub>2</sub> thin films are prepared and they are characterized [10–16]. Recently, SnO<sub>2</sub> thin films are commonly used as a material for the detection of a wide variety

of gases because they are appropriate for physical and chemical aspects and low cost compared to actual materials for the same purpose. At room temperature, the tin oxide sensor is sensitive to certain gases or vapors such as, NH<sub>3</sub>, NO<sub>2</sub>, O<sub>2</sub>, H<sub>2</sub>, CO, NO, and ethanol [17]. Pure SnO<sub>2</sub> acquires some disadvantages such as high operating temperature, low selectivity, and low sensitivity, which must be taken into account before SnO<sub>2</sub>-based equipment is marketed [18]. Normally, appropriate catalysts, noble metals, and transition metals are incorporated into the SnO<sub>2</sub> sensors to boost their sensing response and selectivity [19]. In this work, Neodymium-doped SnO<sub>2</sub> films are prepared by the nebulizer spray pyrolysis method. This method is cost-effective and doesn't require a vacuum. The preparation conditions such as the flow rate and temperature influence the morphology and size of the grains in the prepared films [20].

The prepared films are characterized by energy dispersive X-ray analysis (EDXA) to confirm the chemical compositional nature of the material. The Raman spectroscopy, photoluminescence, and UV–Vis–NIR spectroscopy techniques are employed to study the optical properties of the prepared films. The structural properties of the films are found from the X-ray diffraction technique. The procedure to prepare the undoped and Nd-doped tin oxide films is given in Sect. 2. The results and the corresponding discussion of the characterization techniques are given in Sect. 3 followed by the conclusion.

✉ L. Bruno Chandrasekar  
brunochandrasekar@gmail.com

<sup>1</sup> Department of Physics, Caussanel College of Arts and Science, Muthupettai, India

<sup>2</sup> Thin Film and Nano Science Research Lab, Department of Physics, Alagappa Government Arts College, Karaikudi 630 003, India

<sup>3</sup> Department of Physics, Periyar Maniammai Institute of Science & Technology, Vallam, India

<sup>4</sup> Department of Physics, The American College, Madurai, India

## 2 Experimental procedure

The nebulizer spray pyrolysis method is employed to prepare the SnO<sub>2</sub> films without and with doping. Tin (IV) chloride pentahydrate [SnCl<sub>4</sub>·5H<sub>2</sub>O], Neodymium acetate monohydrate [Nd (CH<sub>3</sub>COO)<sub>2</sub>·H<sub>2</sub>O], and methanol [CH<sub>3</sub>OH] are used to prepare the spray solutions.

Undoped and Nd-doped SnO<sub>2</sub> films are deposited onto glass substrates. For this deposition, 0.1 M precursor solution is prepared by dissolving tin (IV) chloride pentahydrate in methanol. For Nd doping, Neodymium acetate monohydrate is dissolved in the above solution with different concentrations (0, 1, 3 and 5%). Both precursors are easily soluble in the methanol. It is a suitable solvent for nebulizer spray technique because the alcohol solvent can be easily evaporated, so it can reduce the deposition time. Few drops of concentrated hydrochloric acid are added for the complete dissolution of precursors. The final solution is stirred for about 15 min at room temperature to yield a transparent and standardized solution. Before spraying the solution, the glass substrate is cleaned and kept onto the heated plate maintained at constant temperature of 400 °C using a PID temperature controller. A 10 ml precursor solution is used to spray on the substrate at a time. While spraying, the mist formed from the precursor solution is forced to fall on the hot substrate. The spray nozzle is moved slowly over the substrate to spray solution uniformly and get a smooth film. The main parameters maintained during the nebulized spray pyrolysis technique are listed: substrate temperature of 400 °C; substrate to nozzle distance of 25 mm; and carrier gas pressure of 1.0 kg/cm<sup>2</sup>. The prepared films are characterized to study the morphological, optical, micro-structural, and gas sensing properties.

## 3 Result and discussion

### 3.1 Thickness, EDXA, and SEM analysis

The thickness of the film is measured using a profiler technique. The undoped film has a thickness of 320 nm, whereas 5% Nd-doped SnO<sub>2</sub> film has 410 nm. As the doping concentration increases the film thickness also increases. The chemical compositional analysis is done using the EDXA technique. The EDXA spectrum of the films is presented in Fig. 1. The purity of the sample and the presence of the dopant are confirmed in the EDXA spectrum.

The high-resolution SEM images of undoped and 5% Nd-doped tin oxide are shown in Fig. 2. The presence of Sn and O in the undoped films and the dopant Nd in the Nd-doped tin oxide films are shown using different colors in elemental mapping. A small area analysis reveals that the number of green dots is less than the blue and red conforming to the doping level. The image analysis of SEM reveals that the grains are spherical and have got agglomerated due to the thermal energy available on formation of undoped and Nd-doped tin oxide surfaces. The Nd-doped tin oxide films have revealed a smoothened surface feature compared to the undoped.

### 3.2 Raman studies

The optical measurement by Raman spectroscopy is carried out further to determine the characteristics of SnO<sub>2</sub> and Nd-doped SnO<sub>2</sub> films. The Raman spectra of SnO<sub>2</sub> and Nd-doped SnO<sub>2</sub> films are shown in Fig. 3. Rutile SnO<sub>2</sub> belongs to the point group D<sub>4h</sub> with two SnO<sub>2</sub> molecules per unit cell and 15 optical phonons corresponding to this symmetry as given by

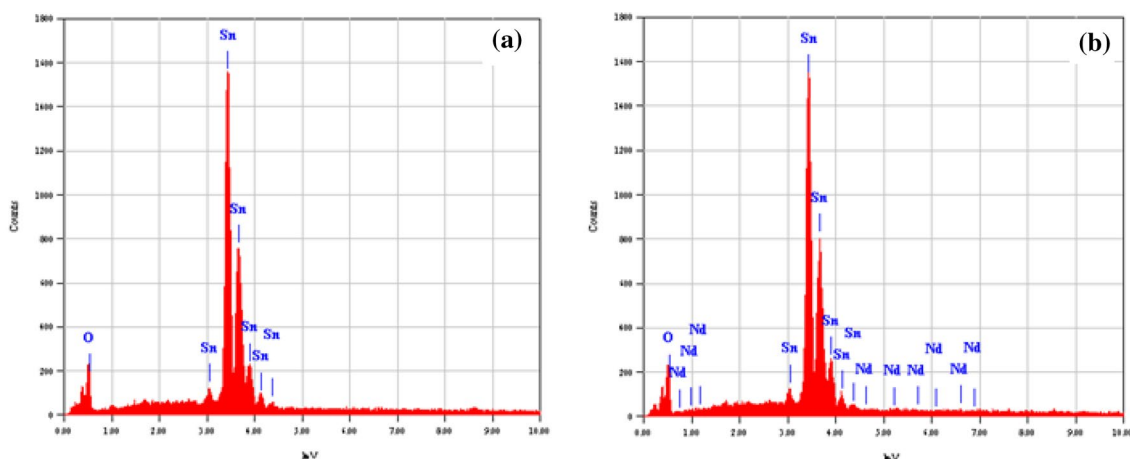
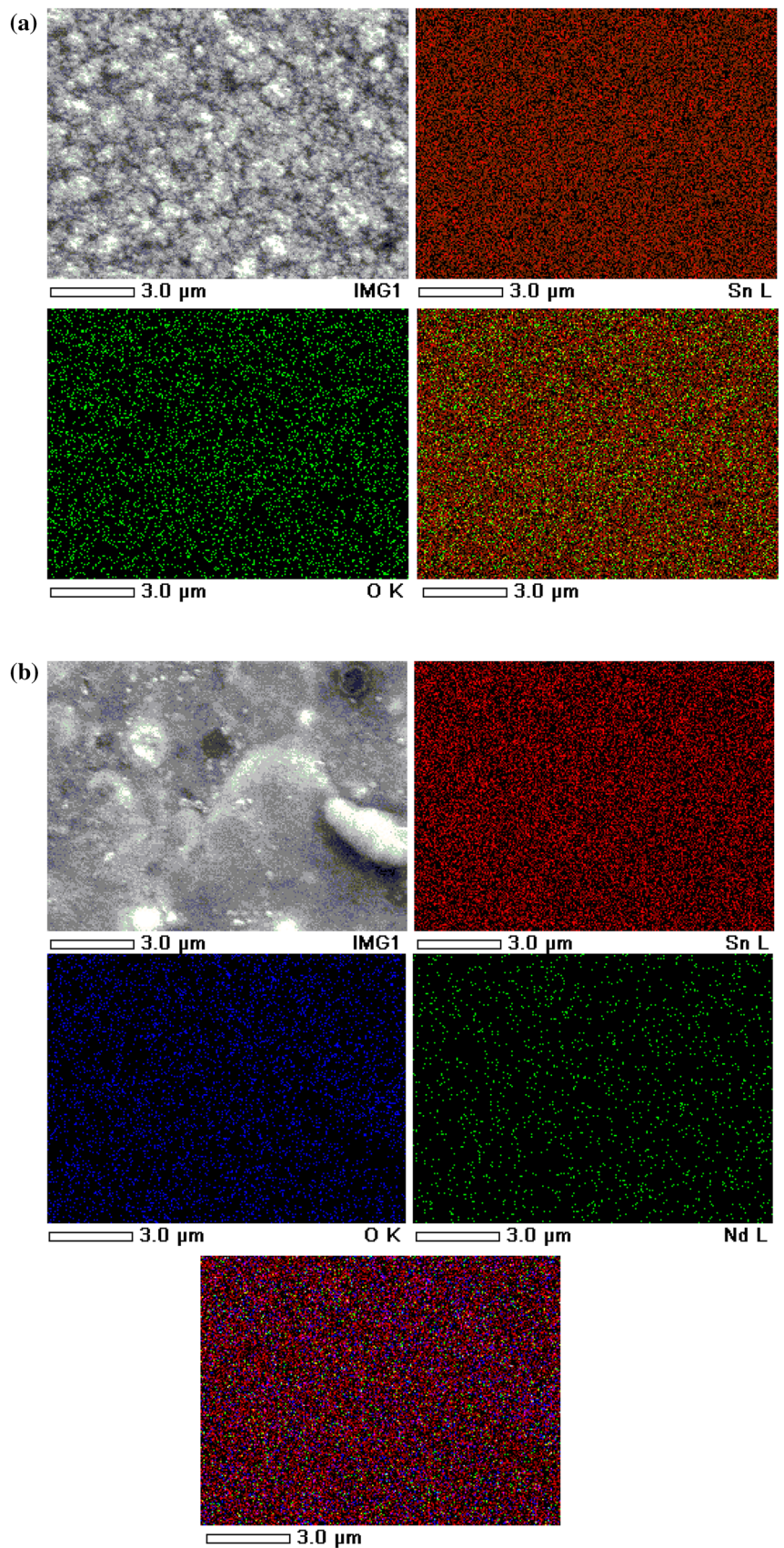


Fig. 1 EDXA Spectrum of **a** undoped and **b** 5% Nd-doped SnO<sub>2</sub> films

**Fig. 2** **a** SEM and elemental mapping image for undoped tin oxide film **b** SEM and elemental mapping image for 5% Nd-doped tin oxide film



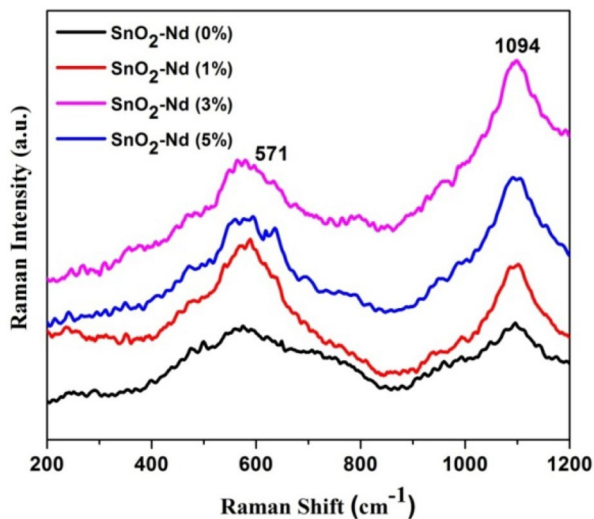


Fig. 3 Raman Spectrum

$$\Gamma = A_{1g} + A_{2g} + A_{2u} + B_{1g} + B_{2g} + 2B_{1u} + E_g + 3E_u$$

where  $A_{1g}$ ,  $B_{1g}$ ,  $B_{2g}$ , and  $E_g$  are Raman active. The spectrum of  $\text{SnO}_2$  shows fundamental Raman-active peaks corresponding to the rutile structure of  $\text{SnO}_2$  at 473, 632, and 773  $\text{cm}^{-1}$ . These Raman shifts are consistent with the  $E_g$ ,  $A_{1g}$ , and  $B_{2g}$  vibration modes, respectively. The  $A_{1g}$  and  $B_{2g}$  modes are non-degenerate and might be related to the expansion and contraction of the vibrating mode of Sn–O bonds, whereas the doubly degenerate  $E_g$  mode may be related to the vibration of oxygen in the oxygen plane. The  $A_{1g}$  and  $B_{2g}$  modes vibrate in the plane perpendicular to the  $c$ -axis, whereas the  $E_g$  mode vibrates in the direction of the  $c$ -axis. In addition to these peaks, the observation of new peaks can be explained based on the quantum confinement effect. In thin films, the surface properties are sensitive not only to the grain size and their distributions but also to the oxygen vacancies and local disorder. So there may be a possibility of the appearance of new modes in the Raman spectra [21–23].

### 3.3 Photoluminescence and UV–Vis–NIR spectroscopy

Figure 4 shows the room temperature photoluminescence spectra for the prepared films recorded in the range of 350–600 nm using 380 nm excitation wavelengths. The undoped films have high intensity than the doped films. The emission spectrum consists of 368, 406, and 471 nm emission peaks. The peak around 370 nm (3.36 eV) is due to the direct band gap transition. The peak at 406 nm (3.05 eV) may be due to the oxygen vacancies in the  $\text{SnO}_2$  lattices. Similarly, the peak at 471 nm (2.63 eV) appeared due to the presence of singly charged oxygen vacancies ( $V_o^+$ ) in the film [24, 25]. The doping of Nd in the Sn lattice highly

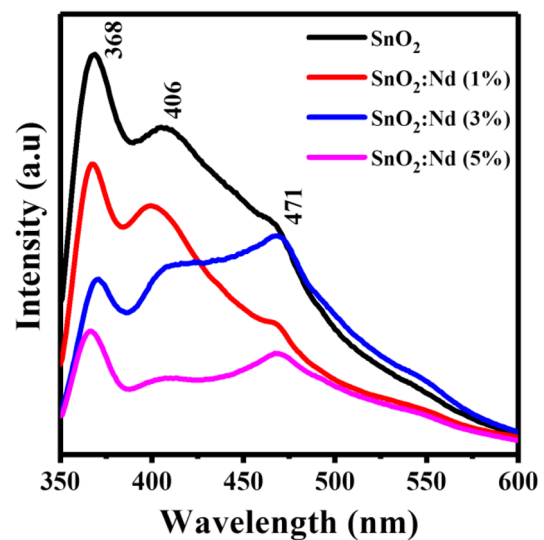


Fig. 4 PL spectrum

influenced the PL spectrum in terms of intensity. The doping concentration reduces the PL intensity and it is due to quenching. The transmittance spectra of the films are recorded from 300 to 1200 nm and are shown in Fig. 5. The undoped films have high transmittance than doped films. As the wavelength increases, the transmittance of the films also increases and reaches saturation. The undoped film reaches the saturation first than doped films in terms of wavelength. The doping reduces the transmittance of the films. Similar results are reported in doped tin oxide films [16]. The variations in transmission of the films are mainly due to interference phenomena.

The band gap of the material is found from the Tauc's plot by plotting  $(\alpha h\nu)^n$  against  $h\nu$ . The Tauc's plot for undoped and doped films is shown in Fig. 6. Since the  $\text{SnO}_2$  is a direct band gap material, the value of the 'n' is chosen as  $\frac{1}{2}$  [26].

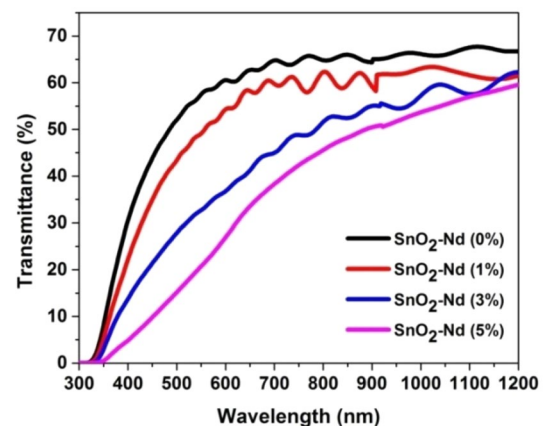


Fig. 5 Transmittance spectrum

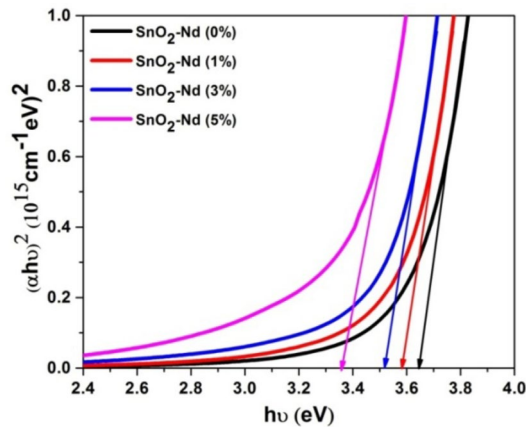


Fig. 6 Tauc plot

The extrapolation of the straight line to the  $h\nu$  axis gives the band gap of the material. For the undoped film, the band gap is higher than the bulk value of 3.6 eV. This similar result is obtained by Deepa et al. [27]. The calculated band gap ranges from 3.64 to 3.35 eV when the doping concentration changes from 0 to 5%, respectively. The undoped films have a high band gap and the doping reduces the band gap. The charge carrier concentration is found from  $E_g^{bulk} - E_g^{film} = \frac{h^2}{8m^*} \left(\frac{3}{\pi}\right)^{2/3} n_e^{2/3}$ , where  $n_e$  is the electron concentration,  $E_g^{film}$  is the band gap of the prepared film, and  $E_g^{bulk}$  is the bulk band gap [28]. The electron concentration increases as the doping concentration of Nd increases. Hence it is clear that the films become more n-type as the doping of Nd increases. Moreover, when the doping concentration increases from 0 to 5%, the electron concentration increases by more than ten times. The refractive index of the films is calculated from the expression [28],

$$\frac{n^2 - 1}{n^2 + 2} = 1 - \sqrt{\frac{E_g}{20}}$$

Here,  $n$  is the refractive index of the material and  $E_g$  is the band gap of the prepared films (in eV). The undoped film has a refractive index of 2.242 and the doping of Nd causes the high refractive index. The calculated band gap, electron concentration, and refractive index are tabulated in Table 1.

### 3.4 X-ray diffraction studies

The Fig. 7 shows the XRD pattern for undoped and doped tin oxide films. All the films show the polycrystalline rutile structure [29]. The recorded XRD pattern is in coincidence with the standard XRD pattern (JCPDS:41-1445) [29]. The effective doping in a tin lattice is confirmed based on the following reasons: (i) the absence of the secondary peaks due

**Table 1** Band gap, electron concentration, and refractive index of the films

Nd concentration (%)	Band gap (eV)	Charge carrier concentration ( $\times 10^{25} / \text{m}^3$ )	Refractive index
0	3.64	0.96	2.242
1	3.58	2.72	2.257
3	3.51	5.42	2.271
5	3.35	13.61	2.306

to Nd or  $\text{NdO}_2$  and (ii) the shift of the Miller planes of the doped films as compared with undoped  $\text{SnO}_2$  films.

As the doping concentration of Nd increases, the intensity of the film also increases. Moreover, the relative intensity between the planes (110) and (101) as well as (101) and (200) depend on the concentration of doping. The grain size of the prepared films is found using Debye-Scherrer's formula as [26]

$$D = k\lambda / \beta \cos\theta$$

where  $k$  is chosen as 0.94,  $\lambda$  is the wavelength of  $\text{Cu-K}\alpha$  line,  $\beta$  is the full width at half maximum and  $\theta$  is the Bragg's angle. The dislocation density is found from  $\delta = \frac{1}{D^2}$  [26] and the strain is found from  $\epsilon = \frac{\beta \cot\theta}{4}$  [30]. The grain size of the undoped film is 16 nm, whereas 5% doped film has a grain size of 33 nm. This is due to the direct fact that the

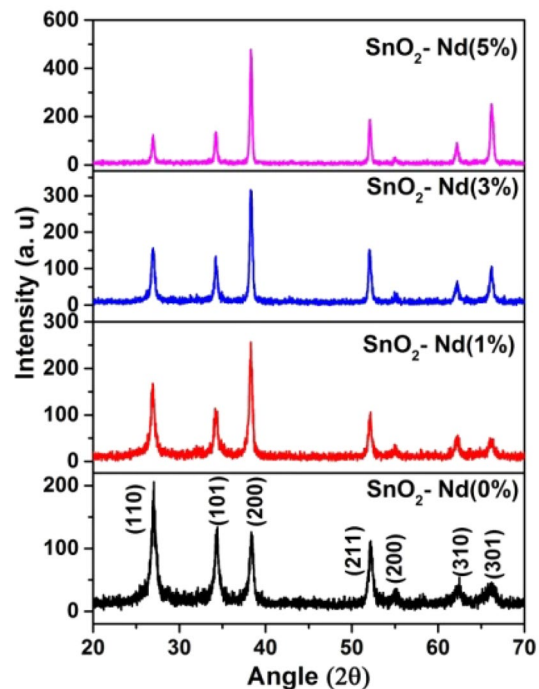


Fig. 7 XRD Pattern

atomic radius of Nd is greater than the atomic radius of Sn. The grain size changes non-linearly due to doping concentration. The dislocation density and the strain of the material decrease as the doping concentration of Nd increases. The thickness and the grain size of the thin films are the key factors in the properties of thin films. The results show that the doping of Nd changes the film thickness and the grain size; hence one can tune the properties of SnO<sub>2</sub> thin films simply by effective doping. The lattice constants for the tetragonal phase structure is found from the standard equations as given in [29]. They are, respectively, given as

$$d^{-2} = \frac{h^2 + k^2}{a^2} + \frac{l^2}{c^2}$$

$$V = a^2c$$

The calculated lattice constants are in coincidence with the standard results and the volume of the unit cell increases due to doping of Nd. All the calculated values are presented in Table 2. Since from our best of knowledge no results are found in the literature to study the role of Nd concentration in SnO<sub>2</sub> thin films, the comparison of our results is not possible.

### 3.5 Ammonia gas sensor analyses

In general, when certain gas molecules are adsorbed, the electrical properties of the semiconductor metal oxides will change. When the material is exposed to an NH<sub>3</sub> environment, metal oxide sensor properties can be detected as the change in electrical resistance. The Keithley electrometer and computer connected homemade sensor setup is shown in Fig. 8. The silver paste is applied for the study of NH<sub>3</sub> vapor sensing characteristics of prepared films in order to create electrical contacts on top of the films.

A particular volume of liquid ammonia is injected with chromatographic syringe into the 5 L gas sensing chamber. After hitting the electric meter study level, the target gas is allowed into the chamber. Then an unexpected change in resistance to baseline suggesting system sensing properties is observed. The differences in resistance are measured continuously. The basic ammonia gas sensing characteristics of

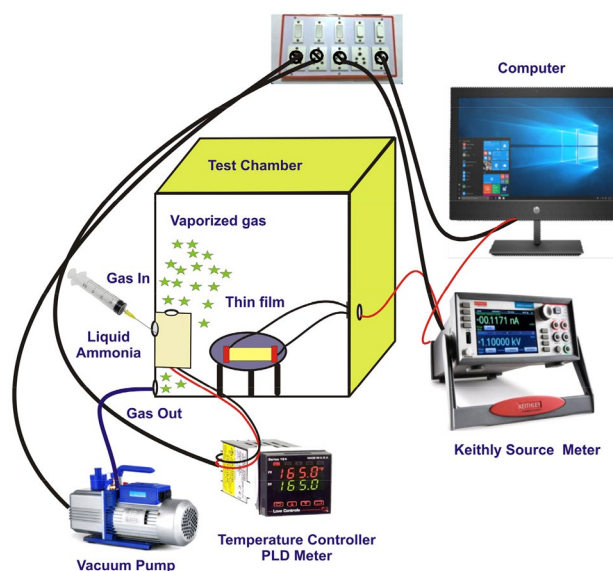


Fig. 8 Gas sensor setup

the prepared films are graphically shown in Fig. 9a–c. When the prepared films are exposed to ammonia, it converts into NO and then it dissociates to nitrogen and oxygen. The oxygen gets electrons to form the film that causes the change in the resistance. From the following relation, the sensitivity (S%) of the fabricated sensors is calculated [31].

$$Sensitivity = \left\{ \frac{R_a - R_g}{R_a} \right\} \times 100\%$$

where R<sub>a</sub> and R<sub>g</sub> are the resistance of the sensor measured in normal air and test gas atmosphere, respectively. The response time (T<sub>res</sub>) is the time taken for the sensor to achieve 90% of the total resistance (adsorbed gas time), and the time taken for the sensor to re-achieve 90% of the resistance (desorbed gas time) is the recovery time (T<sub>rec</sub>) [32, 33]. The observed response and recovery time of the different doping concentration of Nd-doped films for 25 ppm ammonia is given in Fig. 9a. The observed response, recovery time, and sensitivity for the different doping concentration of Nd is given in Table 3. The response and recovery time decreases with the increase in doping Nd concentration

Table 2 Structural properties

Nd concentration (%)	Film thickness (nm)	Crystallite size (nm)	Dislocation density (lines/m <sup>2</sup> )	Strain (× 10 <sup>-3</sup> )	Lattice constants		Cell volume (Å <sup>3</sup> )
					a (Å)	c (Å)	
0	580	12.63	6.259	9.30	4.6394	3.1561	67.93
1	550	15.66	6.120	8.20	4.7004	3.3467	73.94
3	530	20.51	6.118	8.27	4.7197	3.3680	75.02
5	510	23.89	6.117	8.27	4.7197	3.5752	79.64

**Fig. 9** **a** Response time ( $T_{res}$ ) and recovery time ( $T_{rec}$ ) of  $\text{SnO}_2$ :Nd thin films ( $\text{NH}_3$  gas of 25 ppm concentration). **b** Graphical representation of response time ( $T_{res}$ ) and recovery time ( $T_{rec}$ ) of  $\text{SnO}_2$ :Nd thin film ( $\text{NH}_3$  gas of 25 ppm concentration). **c** Gas response in terms of the resistance of  $\text{SnO}_2$ :Nd(5%) thin film. **d** Stability and reproducibility of 5% Nd-doped  $\text{SnO}_2$  film for 25 ppm  $\text{NH}_3$

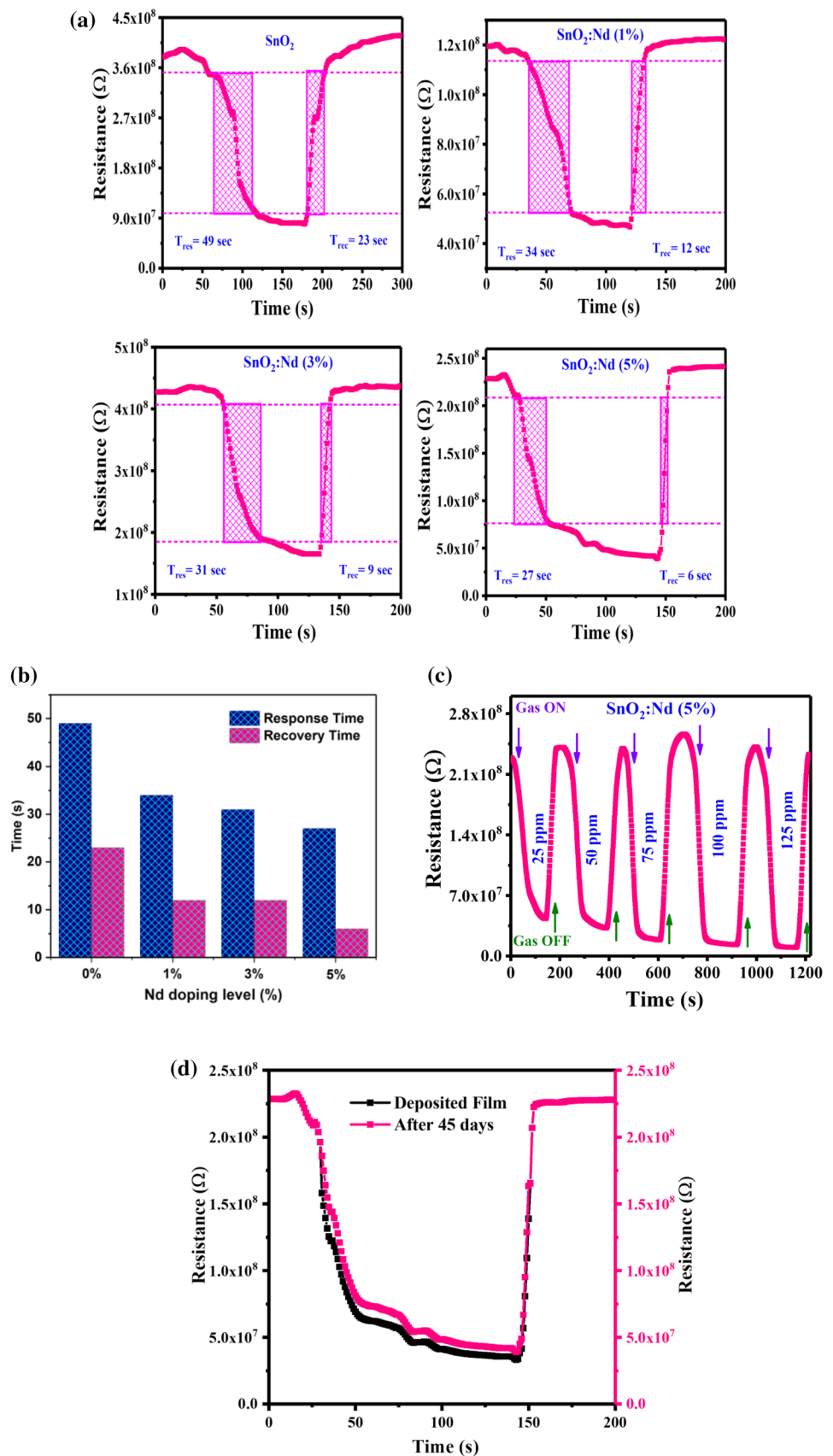


**Table 3** Response time, recovery time, and sensitivity of 5% Nd-doped SnO<sub>2</sub> film for 25 ppm NH<sub>3</sub>

Nd concentration (%)	Response time (sec)	Recovery time (sec)	Sensitivity (%)
0	49	23	58.8
1	34	12	59.7
3	31	9	64.8
5	27	6	68.2

as shown in Fig. 9b. In comparison with other films, the 5% Nd-doped SnO<sub>2</sub> film display the fast quick response (27 s) and fast recovery (6 s) times.

Figure 9c depicts SnO<sub>2</sub>:Nd (5%) thin film response and recovery graph with different ammonia concentrations, such as 25–125 ppm in the step of 25 ppm. It is observed that the resistance gradually increases with ammonia concentration. Hence one can control the gas sensing mechanism simply by the doping of Nd in Sn lattices in SnO<sub>2</sub> films. From the best of our knowledge, a nebulizer spraying technique does not provide a report on the Nd-doped SnO<sub>2</sub> vapor sensor at room temperature. The uniqueness of this work should, therefore, be highlighted and parameters should compared with SnO<sub>2</sub>-based sensors obtained. Yude Wang et al. [34] reported an ammonia sensor at 100 ppm that showed a response time at ~3.3 min and recovery time at ~3 min at 79 °C for the SnO<sub>2</sub>/Sb nanostructure. Deshpande et al. [35] synthesized enhancement of 300–500 ppm NH<sub>3</sub> gas sensor based on SnO<sub>2</sub>/PANI by solution route technique. They showed that tin oxide-intercalated polyaniline exhibited quick response/recovery timings of ~12–15 s/80 s for operating temperature of 300 °C. Sanju Rani et al. [36] investigated the influence of Fe doping on NH<sub>3</sub> sensing by SnO<sub>2</sub> thin film at the operating temperature of 200 °C. It displayed 46% sensitivity towards 1000 ppm gas concentration. In this case, we have achieved response (27 s), recovery time (6 s), and sensitivity of 68.2% for SnO<sub>2</sub>: Nd (5%) at room temperature with ammonia of 25 ppm.

### 3.6 Stability and reproducibility

The quality of the system is controlled by stability and reproducibility. After 45 days, a film has been examined for its efficiency. Particularly, in environmental laboratory conditions, the film is stored. Figure 9d demonstrates the reproducibility of 5% Nd-doped SnO<sub>2</sub> film, which is stored in 25 ppm of ammonia as deposited film and after 45 days. From Fig. 9d, it is evident that the fresh film electrical resistance and the 45 days aged film remains nearly equal ( $3.72 \times 10^7$  for fresh film and  $3.09 \times 10^7$  for aged one). The NH<sub>3</sub> molecule interacts as before with Nd-doped SnO<sub>2</sub>, and thus, the film properties are not influenced by aging. The

consistency and existence of the Nd-doped SnO<sub>2</sub> film in open atmosphere are exceptional from this observation. We conclude from this analysis that the sensing response of the SnO<sub>2</sub> film to ammonia is nearly stable and those films can be further studied with regard to their potential use in the sensing of various gases and for the development of devices.

## 4 Conclusion

Spray pyrolysis method is employed to prepare the undoped and doped SnO<sub>2</sub> films. The thickness of the films, morphological, optical, structural, and gas sensing properties depend on the doping concentration of Nd. The doping is confirmed by the color contrast SEM image and the shifting if the miller plane is in the XRD pattern. The doping reduces the PL intensity and the transmittance of the films. The red-shifted band gap is observed due to doping from the Tauc's plot. Ammonia gas is sensed using these films and its response is presented. This work is extended to study other gases such as H<sub>2</sub>O<sub>2</sub> and O<sub>3</sub>.

## References

1. L. BrunoChandrasekar, P. Raji, R. Chandramohan, R. Vijayalakshmi, G. Devi, P. Shunmugasundaram, P. Sindhu, J. Nanoelectron. Optoelectron **8**(4), 369–372 (2013)
2. L. BrunoChandrasekar, M. Karunakaran, K. Gnanasekar, Commun. Theor. Phys. **71**(3), 339–343 (2019)
3. N. Liu, M. Chen, M. Ran, C. Zhang, X. Luo, H. Lu, Y. Yang, Opt. mat. Express **10**, 157, (2020)
4. L. BrunoChandrasekar, S. Nagarajan, P. Ramasundari, R. Vijayalakshmi, M. Karunakaran, T. Daniel Thangadurai, J. Optoelectron Adv M, **21**, 146–150, (2019)
5. D.H.O. Machado, L.V.A. Scalvi, C.F. Bueno, Condens. Matter **2**, 9 (2017)
6. E. Boyal, V. Baran, T. Asar, S. Ozcelik, M. Kasap, J. Alloys Compd. **692**, 119 (2017)
7. S. Gurakar, T. Serin, N. Serin, Appl. Surf. Sci. **352**, 16 (2015)
8. Y. Zuo, S. Ge, L. Zhang, S. Yan, X. Zhou, Y. Xiao, J. Alloys Compd. **475**, 60 (2009)
9. G. Bhatia, V.K. Gupta, M.M. Patidar, S.B. Srivasatava, D. Singh, G. Mohan, V. Ganesan, AIP Conference Proc. **1953**, 100084 (2018)
10. M.J. Powell, BAD Williamson, B. Song-Yi, J. Manzi, DB Potter, DO Scanlon, CJ Carmalt, Chem. Sci. **9**, 7968, (2018)
11. Y. Cho, N.S. Parmar, SahnNahm, C. Ji-Won, J. Alloys. Compd **694**, 217–222 (2017)
12. S. Haya, O. Brahmia, O. Halimi, M. Sebais, B. Boudine, Mater. Res. Express **4**, 106406 (2017)
13. KA Bogle, KD More, S Begum, JW Dadge, MP Mahabole, RS khairnar, Indian J. Pure Ap.Phys. **56**, 755, (2018)
14. P. Kumar, K. Kumari, M. Sharma, P.A. Alvi, S. Kumar, AIP Conf Proc **2006**, 030039 (2018)
15. N. Nanda Kumar Reddy, H. Sharma Akkera, M. Chandra Sekhar, P. Si-Hyun, Appl. Phys. A, **123**, 761, (2017)
16. Q.P. Tran, J.S. Fang, T.S. Chin, Mat. Sci. Semicond. Process. **40**, 664 (2015)



17. M.H. Diwan, W.M. Kadem, Z.T. Khodair, AIP Conf Proc **2144**, 030010 (2019)
18. G. Singh, Virpal, Ravi Chand Singh. Sens. Actuators B Chem **282**, 373–383 (2019)
19. Wu Yuemei, H. Zhang, Y. Liu, W. Chen, J. Ma, S. Li, Z. Qin, J. Sens. **15**, 14230–14240 (2015)
20. TV. Gavrilovic, DJ. Jovanovic, MD. Dramicanin, Nanomaterials for green Energy, 55, 81, (2018)
21. R.S. Katiyar, P. Dawson, M.M. Hargreave, G.R. Wilkinson, J. Phys. C: Solid State Phys. **4**, 2421 (1971)
22. R.N. Mariammala, K. Ramachandran, B. Renganathan, D. Sastikumar, Sens. Actuators B **169**, 199–207 (2012)
23. D.L. Hou, H.J. Meng, L.Y. Jia, X.J. Ye, H.J. Zhou, X.L. Li, Phys. Lett. A **364**, 318 (2007)
24. K. Thirumurugan, K. Ravichandran, R. Mohan, S. Snega, S. Jothiramalingam, R. Chandramohan, Surf Eng **29**(5), 373–378 (2013)
25. K. Ravichandran, K. Thirumurugan, J. Mater. Sci. Technol. **30**(2), 97–102 (2014)
26. L. Bruno Chandrasekar, S. Nagarajan, P. Ramasundari, R. Vijayalakshmi, M. Karunakaran, T. DanielThangadurai, J. Optoelec. Adv. Mater. **21**, 146, (2019)
27. S. Deepa, B. Thomas, K. PrasannaKumari, J. Mater Sci-Mater. El, **30**, 16579, (2019)
28. T.A. Vijayan, R. Chandramohan, S. Valanarasu, J. Thirumalai, S.P. Subramanian, J. Mater. Sci. **43**, 1776 (2008)
29. N.N.K. Reddy, H.S. Akkera, M.C. Sekhar, S.H. Park, Appl. Phys. A **123**, 761 (2017)
30. C.S. Prajapati, P.P. Sahay, Appl. Surf. Sci. **258**, 2823–2828 (2012)
31. K. Govardhan, A. Nirmala Grace, J. Sens. Vol 2016, Article ID 7652450, p. 12
32. K. Deva Arun Kumar, S. Valanarasu, JS. Ponraj, BJ. Fernandes, M. Shakir, S. Alfaify, P. Murahari, K. Ramesh, J Phys Chem Solids, 144, 109513, (2020)
33. K. Khun Khun, A. Mahajan, RK. Bedi, J. Appl. Phys. **106**, 124509, (2009)
34. Y. Wang, Q. Mu, G. Wang, Z. Zhou, Sens. Actuators B **145** 847–853, (2010)
35. NG Deshpande, YG Gudage, R. Sharma, JC Vyas, JB Kim, YP Lee, Sens. Actuators B **138**, 76–84, (2009)
36. S. Rani, SC. Roy, MC. Bhatnagar, Sens. Actuators B, **122**, 204–210, (2007)

**Publisher's Note** Springer Nature remains neutral with regard to jurisdictional claims in published maps and institutional affiliations.